ASSESSING SEISMIC UNCERTAINTY VIA GEOSTATISTICAL VELOCITY MODEL PERTURBATION AND IMAGE REGISTRATION: AN APPLICATION TO SUB-SALT IMAGING

Lewis Li[1], Jef Caers[1], and Paul Sava[2]

INTRODUCTION

The advent of 3D, wide azimuth reflection seismology has dramatically improved seismic image quality, and allowed the upstream oil industry to image potential targets located beneath complex overburden. This has opened new avenues for subsalt exploration, and salt basins such as those located in the Gulf of Mexico and in the Brazilian offshore have recently been the site of huge discoveries. Despite the improvements in seismic technology, the resulting images are still often poor, especially in the regions around and beneath the salt body. As a result, there will often be large uncertainties in the positioning of horizons and faults, especially in the subsalt layers as shown in Figure 1. Interpretation and subsequent structural and petro-physical modeling is performed using this uncertain seismic image, and can yield unreliable and widely varying reserve estimates. This will have significant effects on exploration, development and drilling decisions.

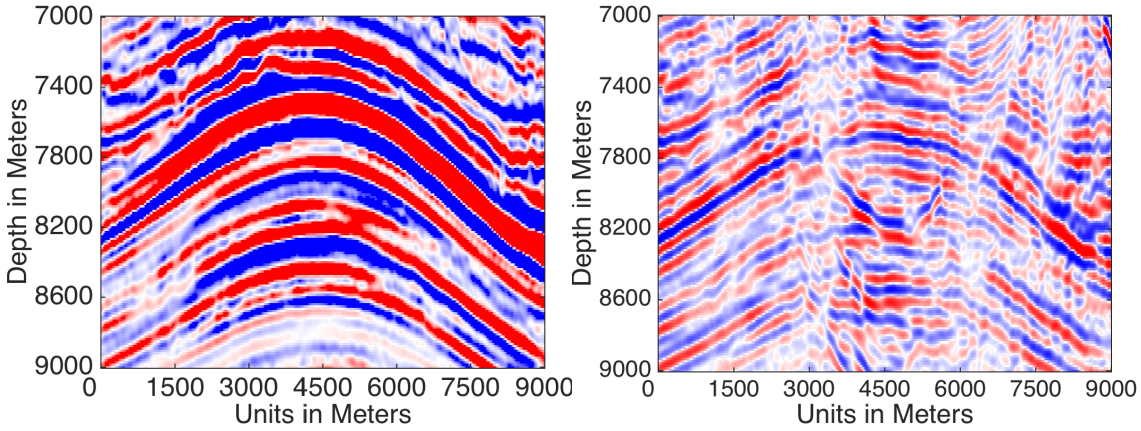


Figure 1: Migrated Images of an anticline from the SEAM Model located beneath complex overburden. The left is the true image of the structure, while the right indicates a typical image that can be reasonably obtained from an estimate of the velocity model.

The physical reason behind this uncertainty is the irregularity of the salt geometry, which causes the seismic waves to scatter and refract, resulting in poor illumination of the subsalt structures. This poses significant challenges for the construction of accurate velocity models, required for depth migration. Compounding this problem is that due to the computational and manual labor costs associated with tomography, only a single velocity model is usually produced, and therefore any uncertainties in the velocities are neglected. Rather, uncertainty is only considered after

[1] Department of Energy Resources Engineering, Stanford University, Stanford, CA

[2] Department of Geophysics, Colorado School of Mines, Golden, CA

interpretation, and during structural modeling. Common workflows such as (Thore, Shtuka, Lecour, Ait-Ettajer, & Cognot, 2002) and (Mallet , 2014), stochastically perturb the interpreted faults and horizons around this single *best-guess* or *preferred* interpretation. However, pitfalls associated with these approaches include difficulties in quantifying the perturbation magnitude, and the unsubstantiated assumption that structural uncertainty should be centered on the preferred interpretation.

This paper outlines a new geostatistical framework to assess 3D velocity model uncertainty, and its implications on modeling structural uncertainty. It can be seen as an extension of existing uncertainty assessment workflows, as shown in Figure 2. The main conceptual difference is that we no longer consider the best guess model to be a *preferred* model, but rather use it an *initial* model to generate an ensemble of randomized velocity models that are verified to be consistent with observed geophysical data. To mitigate the computational costs of performing migration on a large set of velocity models, a model selection procedure is developed for choosing a subset representative of the uncertainty of the full Monte Carlo. Finally, the uncertainty of the imaged seismic events is assessed using image registration techniques. While the workflow is illustrated using the SEG Advanced Modelling (SEAM) model, which contains a large complex salt structure, the framework itself can be extended to other geological scenarios and settings.

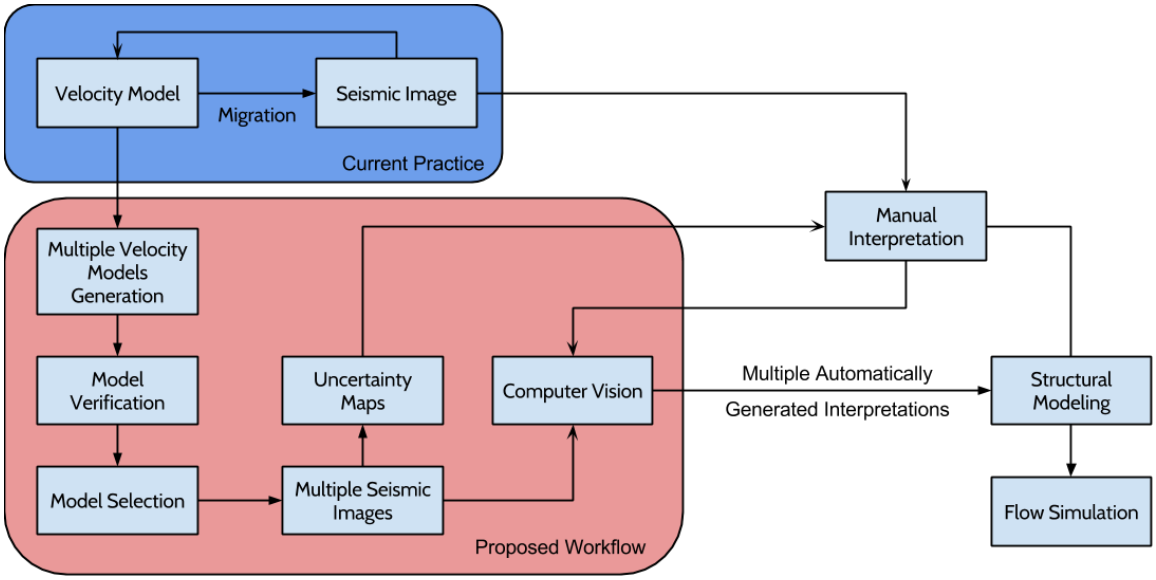


Figure 2: Proposed workflow for combining existing seismic tomography workflows with geostatistical velocity model generation and image registration to assess seismic imaging uncertainty.

GEO-STATISTICAL MODEL GENERATION

Tomographic inversion has been known to be an ill-posed problem for decades, and attempts to circumvent this have generally involved regularization or eigen-decomposition. However, these techniques are generally computationally expensive, and generate overly smooth velocity functions (Osypov, et al., 2013). (Clapp, 2004) proposed a method using the Dix equation to construct multiple velocity realizations to assess structural uncertainty. This method is suitable for 1D smoothly varying velocities and cannot account for large velocity contrasts such as in the case of salt or any other complexity in the overburden structure.

In subsalt imaging, the uncertainty in the velocity model is dominated by the uncertainty in the salt body geometry. A geostatistical approach to capturing this would require generating a set of salt geometries, which to a modeler would appear as realistic as the reference geometry. This entails maintaining physical attributes of the salt among the resulting realizations. For instance, salt tectonics suggests that the top salt surface will have a very high rugosity. Delineating such small-scale rugosities in the velocity model is a highly difficult task; rather, we aim to stochastically generate a set of realizations with the same rugosity, but still geometrically unique. To this end, the salt body is modelled as a fractal with a spatially varying fractal dimension that describes the local rugosity. This is estimated by computing the local Minkowski-Bouligand dimension (Schroeder , 1991) on the initial salt geometry.

The other difficulty associated with subsalt imaging concerns poor and uneven illumination. The large velocity contracts between the salt top and its surrounding sediments will cause a wavefield to defocus as it passes through the salt. These two issues cause holes in the illumination patterns subsalt. Poorly illuminated regions of the initial velocity such as the dipping regions and the under side of the salt body are more uncertain than properly illuminated regions (Figure 3). To model this, we propose the concept of an uncertainty buffer, i.e. an envelope that encloses the surface of the reference salt geometry. This uncertainty buffer represents the region where the salt boundary *could* be, and will vary in thickness spatially. The shape and size of the buffer should also be verified by a human interpreter, which allows the injection of expert opinion into the procedure.

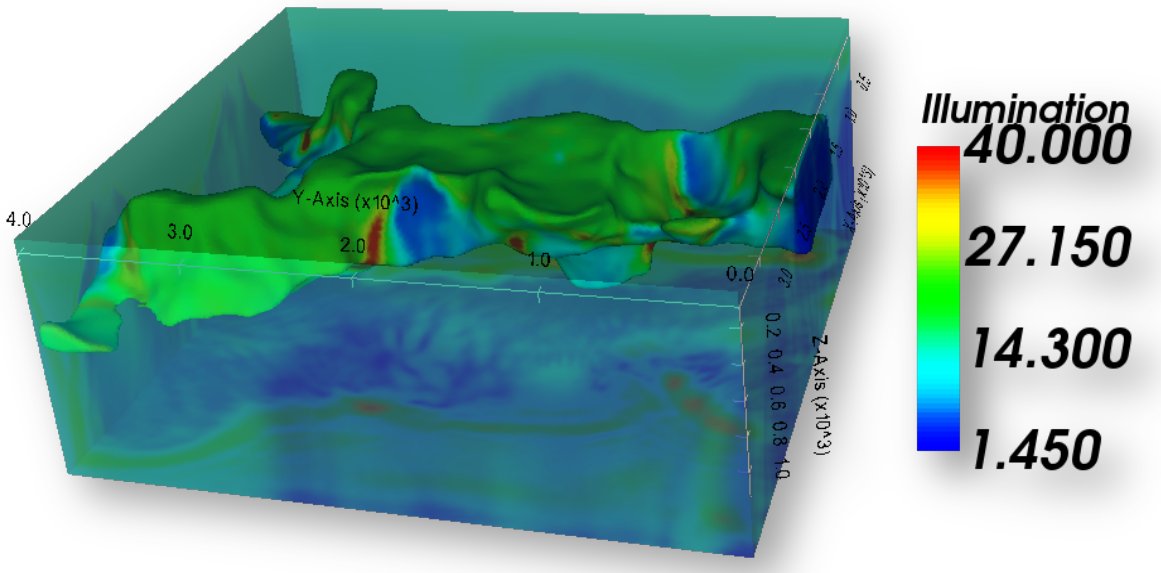


Figure 3: Regions of the salt body with poor illumination will be more uncertain than well-illuminated regions. The illumination is computed using the initial velocity model and is used along with expert opinion to define an uncertainty buffer around the initial model describing where the salt boundary could be.

The geostatistical method is designed such that it samples salt-boundary surface realizations contained within this uncertainty buffer, while maintaining the rugosity of the surface. To achieve this, a fractal generation problem is formulated. We introduced a 2D method in (Li, Sava, & Caers, 2014), by which the reference salt geometry is characterized as a contour and perturbed. To extend this to 3D, we will characterize the salt body as a surface, and use a modified version of the Perlin Noise algorithm (Perlin, 2002) to generate realizations. The Perlin Noise algorithm is a procedural method developed for simulating realistic textures for computer graphics. The basic idea is the generation of a series of pseudo random fields (termed octaves), each with increasing spatial frequency, but decreasing amplitude. By taking the superposition of these fields, a single spatially correlated random field is generated. The initial model is then perturbed according to this generated random field. The increase in spatial frequency between octaves determines the rugosity of the final realization, and thus is controlled by the fractal dimension as shown in Figure 4. By scaling the amplitudes according to the local size of the uncertainty buffer, we constrain the resulting realizations to being within the buffer, and induce variation according to the local variability. Lower octaves exhibit more variation in poorly illuminated regions, while higher octaves induce rugosity in the rougher regions.

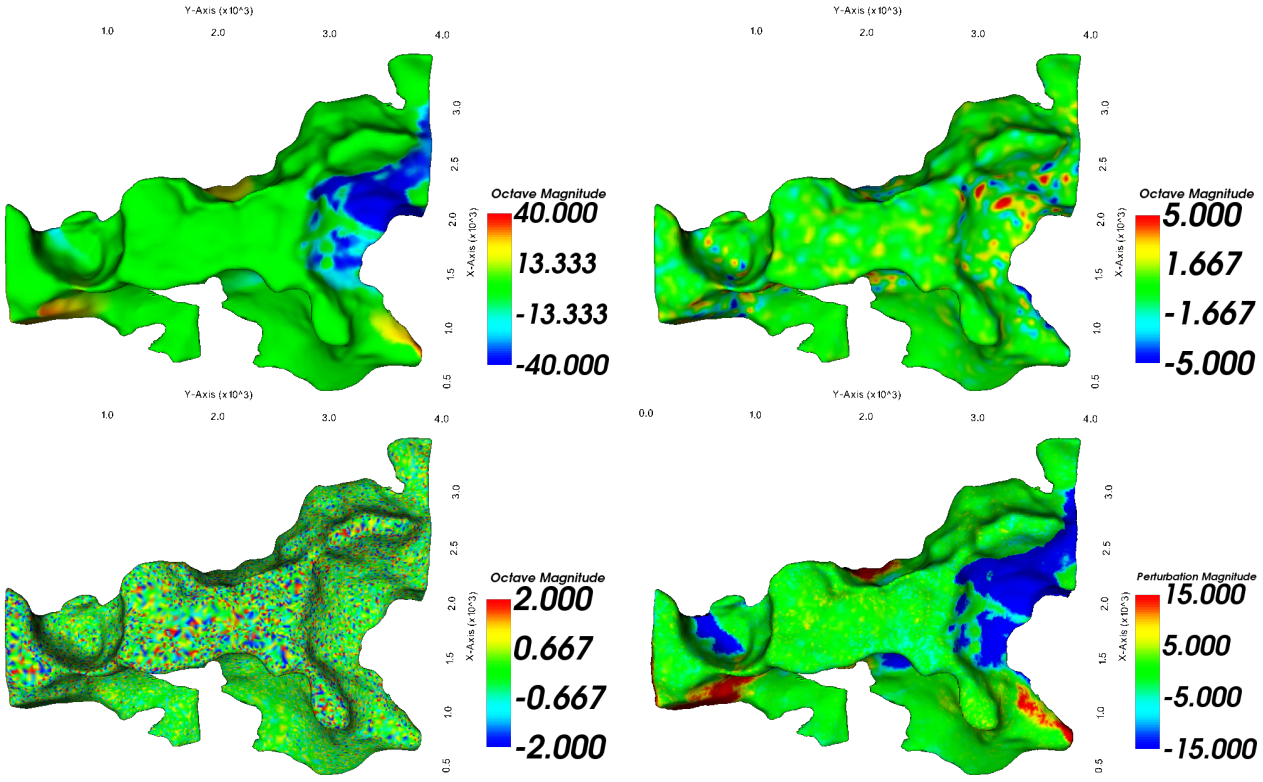


Figure 4: Sample octaves generated using the Perlin noise algorithm. Each octave has increasing spatial frequency but decreasing amplitude. The bottom right image is the superposition of 6 octaves. The initial salt geometry is then displaced by the generated magnitude.

Multiple runs of the modified Perlin noise algorithm will produce realizations of the salt geometry that maintain the same surface rugosity in a statistical sense, while sampling the uncertainty buffer. For instance, the poorly-illuminated regions will exhibit more variation between realizations than well-illuminated regions. A voxelization algorithm is then applied to convert the perturbed salt

geometry surface back onto a Cartesian grid. This method is computationally efficient, as each realization taking less than a second to generate.

Model Selection and Verification

Using salt geometry and velocity model generation algorithm described in the previous section, thousands of 3D realizations can be generated within a few minutes. However, before performing depth migration with these models, two issues must first be address: a) the verification that the generated models are in accordance with observed geophysical data, and b) the computational bottleneck associated with migrating data with thousands of velocity models. The first issue is commonly studied in Migration Velocity Analysis (MVA), and some of the popular methods involve examining the flatness of reflectors in the Common Image Gathers (CIG). There has a great deal of research in tomographic corrections (refer to Chapter 12 of (Biondo, 2005)), but in our particular application, the ability to generate many model quickly, allows for rejection sampling. To avoid performing any migration for model verification, gravity models are used as a computationally faster alternative. Rock physics relations such as Gardner's Relation are used to transform the generated velocity models into density models on which gravity anomalies are estimated (Figure 5). By comparing the modeled anomalies to observed gravity data, realizations that deviate too far are rejected. Likewise, magnetic data could be used in a similar fashion.

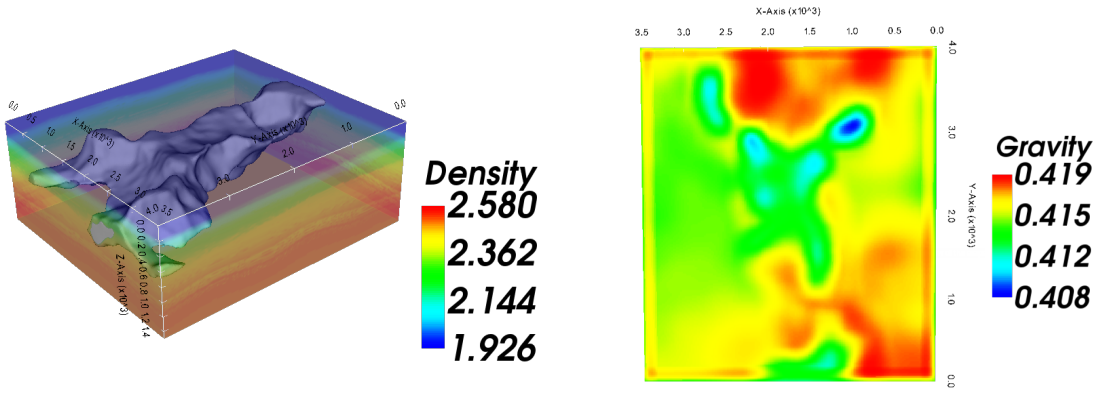


Figure 5: Gravity modeling is used as an faster alternative to migration to verify model consistency. In this example, Gardner's Relation is used to transform a generated velocity model into a density cube (left), on which the gravity anomaly is modeled (right). This is compared to the gravity anomaly of the initial model or observed gravity data if available (additional corrections such as Bouguer need to be applied for comparison with observed). Any generated models that deviate too much are rejected.

The product of the model verification is a large ensemble of velocity models that are in accordance with the observed geophysical data. However migrating seismic data with all of these realizations is computationally infeasible. To address this issue, we apply the distance based model selection method from (Scheidt & Caers, 2009), to select a representative subset of the 3D velocity models for migration (Figure 6). The underlying principle of this method is the definition of a scalar distance between the realizations, using a proxy function that is fast to compute, but is still indicative of the realization variation. One possible such function is the RMS difference between the modeled gravity anomaly. The distances are then tabulated into a distance matrix of dimension NxN, where N is the number of realizations. We then cluster the realizations together according to their distance to each other. However, this is very difficult in N dimensions, and thus Multidimensional Scaling (MDS) is used to project the realizations into a lower dimension while preserving the computed proxy distances. In this lower dimension, the K-medoids clustering algorithm is applied, and a realization

from each cluster is selected as a representative. This gives the modeler the flexibility of migrating as many realizations as time permits.

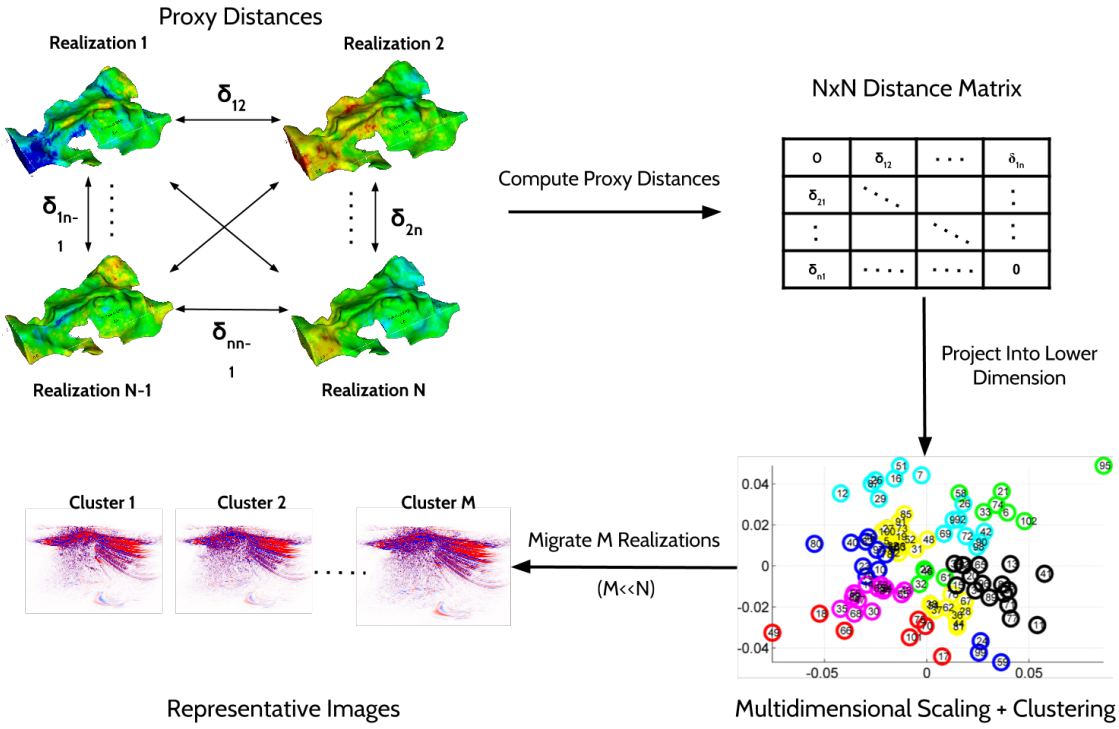


Figure 6: Workflow to select a representative subset of verified velocity models for migration. This allows modelers to select M realizations out of a set of N for forward modeling.

Uncertainty Maps

We described in the previous sections how a representative set of feasible velocity models is generated and selected; thus the next step is to perform migration. Generally, Wave Equation Migration (WEM) or Reverse Time Migration (RTM) techniques (Baysal, Kosloff, & Sherwood, 1983) are preferred for subsalt imaging applications due to the limitations of ray-based schemes for handling multi-pathing caused by sharp velocity contrasts around salt bodies. For demonstration, we migrated with the generated velocity models using split step Fourier one-way WEM (Stoffa, Fokkema, de Luna Friere, & Kessinger, 1990). Undoubtedly, the set of resulting seismic images will vary, as the salt will induce distortions and artifacts, whose shape will vary as the salt geometry is altered. Intuitively, the features whose shape or positions vary the most among the images are those most sensitive to the salt geometry, and therefore the ones that are most likely to be uncertain. Consequently, by computing the voxel-by-voxel distance between the result images, an uncertainty map is generated, indicating regions of higher uncertainty. Depending on which metric is used to compute the distance, different types of uncertainty can be assessed. In (Li, Sava, & Caers, 2014), we showed that the Euclidean distance evaluates the regions where positional uncertainty is highest. Conversely, the Procrustes distance (Appendix A.1), a measure of shape variation, enables highlighting regions where the feature shapes vary the most, and thus the areas where artifacts are

more prevalent. To illustrate this, we generated and imaged 100 realizations of the target anticline in Figure 1, and computed the uncertainty maps shown in Figure 7. These maps suggest that the greatest positional uncertainty is found near the center of the anticline, while the greatest feature shape uncertainty is found along the downward curving structures. These observations are consistent with the deviations in structural positions and artifacts when comparing the true image to

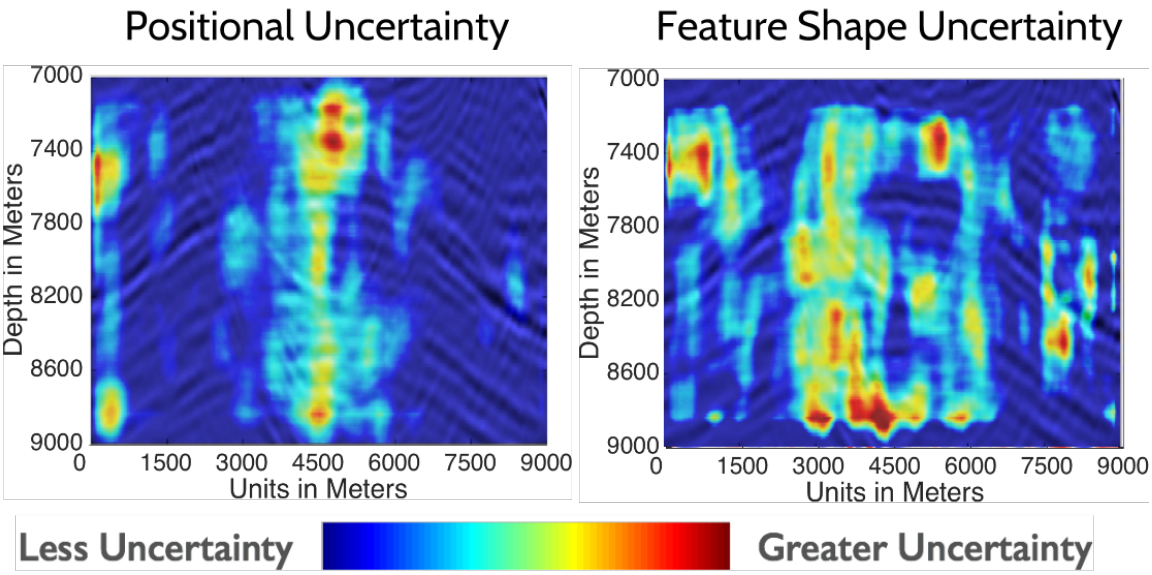


Figure 7: Uncertainty maps produced by comparing the voxel-wise difference between migrated images from the geostatistical generated velocity models.

the image obtained from the initial velocity model (Figure 1). For instance, the position of the anticline's hinge varies more between the initial velocity image and the truth than the limbs. Furthermore, the downwards-dipping structures in the initial image are correctly highlighted as artifacts.

IMAGE REGISTRATION

While the uncertainty map is able to provide an interpreter a qualitative assessment of the positional and structural uncertainty, it does not provide the structural modeler with an assessment of how much horizons should be perturbed when studying structural uncertainty. Ideally, manual interpretation would be performed on the generated seismic images, but this is unfeasible due to the labor costs required. Instead, we propose an approach that requires only a single manual interpretation to be performed, and capitalize on image registration techniques to automatically map the interpretation onto the other seismic images. Image registration is commonly used in medical imaging, for applications such as tracking tumors in MRI scans as the patient inhales and exhales. The objective of registration is to compute the voxel to voxel transformation required to map the *starting* image (on which manual interpretation is performed) to the *target* image (rest of the ensemble of seismic images). The variation among the velocity models causes the migrated images to be both translated and deformed from each other, two separate steps are required to recover the transformation between any two images. The translation between two images is estimated using a simple Phase Correlation (Appendix A2). The remaining difference is modeled as a non-rigid deformation. One of the most popular methods for estimating this deformation is Thiron's Demon

algorithm (Thirion , 1998). Thiron views this deformation as a diffusion process, by which actuators on the starting image (termed Demons after Maxwell's thermodynamic thought experiment) pull the image towards the target image. In mathematical terms, this is a second order gradient descent method with the sum of square of images intensity differences between the starting image *s* and the target image *t* as the criterion (Equation 1).

$$\vec{\mathrm{T}} = (t-s)\times\left(\frac{\vec{\nabla}s}{\left|\vec{\nabla}s\right|^2+(t-s)^2}+\frac{\vec{\nabla}t}{\left|\vec{\nabla}t\right|^2+(t-s)^2}\right)$$

EQUATION 1: Function for estimating deformation between starting image *s* and target image *t*.

This is an iterative algorithm by which the deformation grids T_x, T_y and T_z are continuously applied to ***s***, and recomputed. Interpolation is applied if sub-voxel deformations are computed. This is repeated until a convergence criterion (difference between successive iterations) is met. Figure 8 shows an illustration of using the Demon algorithm to compute the deformation between two images. After 50 iterations, the starting grid is deformed to closely resemble the target grid.

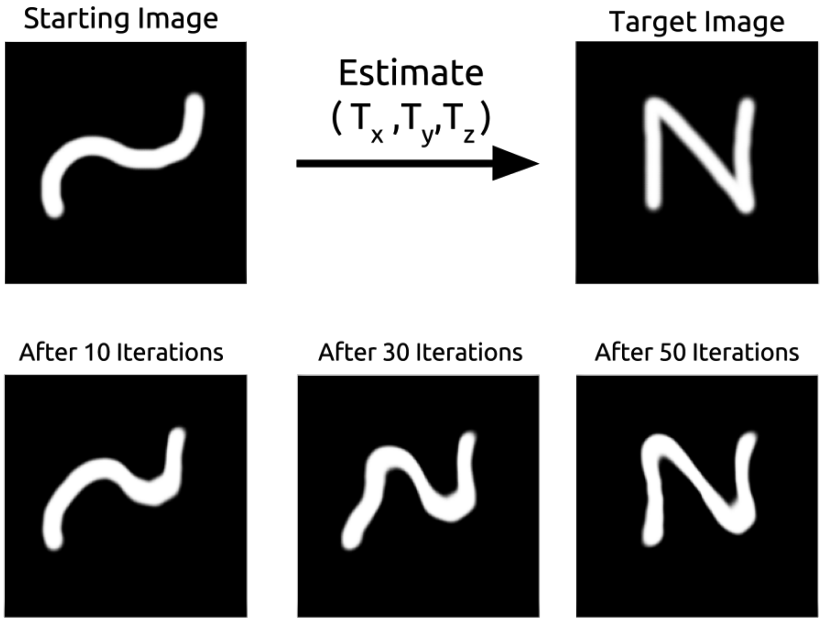


Figure 8: Demonstration of using the Demon Algorithm to deform the starting image into the target image.

The same procedure is applied between the migrated images. One image is chosen from the set of migrated images, and the Demons algorithm is used to compute the deformation between the selected image and the rest of the images in the ensemble. A manual interpretation is performed on the selected image, and deformed by each of the estimated deformations. This yields a set of interpretations on the rest of the images. In our example, a manual interpretation was performed on the image generated from the initial velocity model, and then mapped onto each of the 100 images used to generate the uncertainty maps in the previous section resulting in interpretations such as the

one indicated in Figure 9. This set of interpretations now provides a quantitative assessment of where an interpreted horizon could be located.

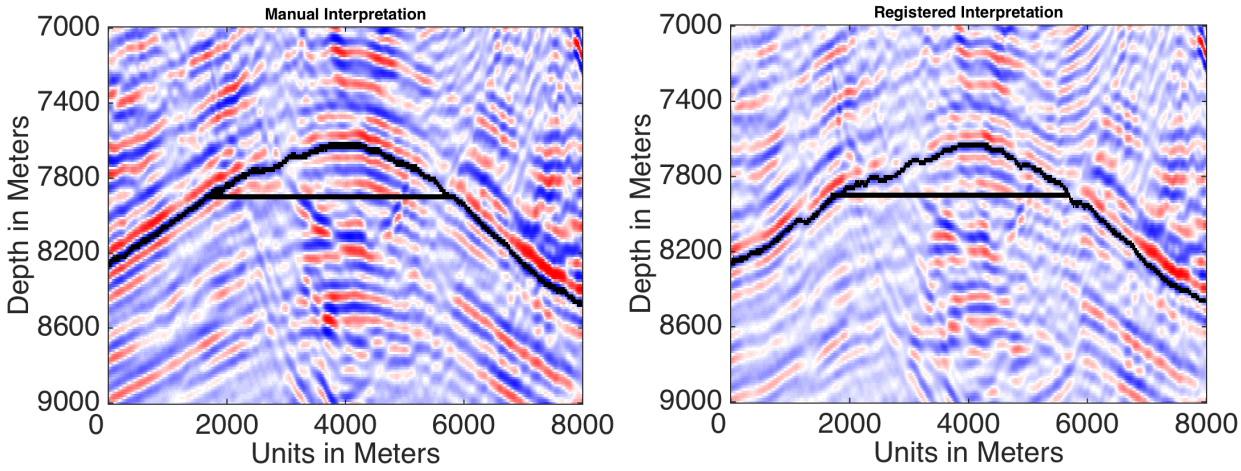


Figure 9: Manual Interpretation (right) and automatically registered interpretation (left) on another image migrated using a perturbed velocity model.

The ultimate goal of uncertainty studies is to provide estimates on the distribution of reservoir properties such as target zone volume, target depth, etc. For sake of illustration, we assumed that the oil water contact was known to be at a depth of 7900m, and computed the target zone area over the set of 100 realizations (Figure 9). We also performed the interpretation on the truth image and indicated the computed area with the red line, while the green line indicates the estimate obtained from migrating the reference velocity model (Figure 10). It should be noted that the distribution of estimates is neither Gaussian nor centered on the estimate obtained using the initial velocity model, serving as a cautionary counterexample to common uncertainty modeling assumptions. Moreover, we see a wide span of uncertainty even for a 2D simplified example. This analysis is extended to 3D (Figure 11), where the Demons algorithm is used to generate alternative interpretations of a section of a target structure. The true structure position is shown in red, and it can be seen that the alternative interpretations do span the true position. These alternative interpretations can then serve as input for structural modeling workflows.

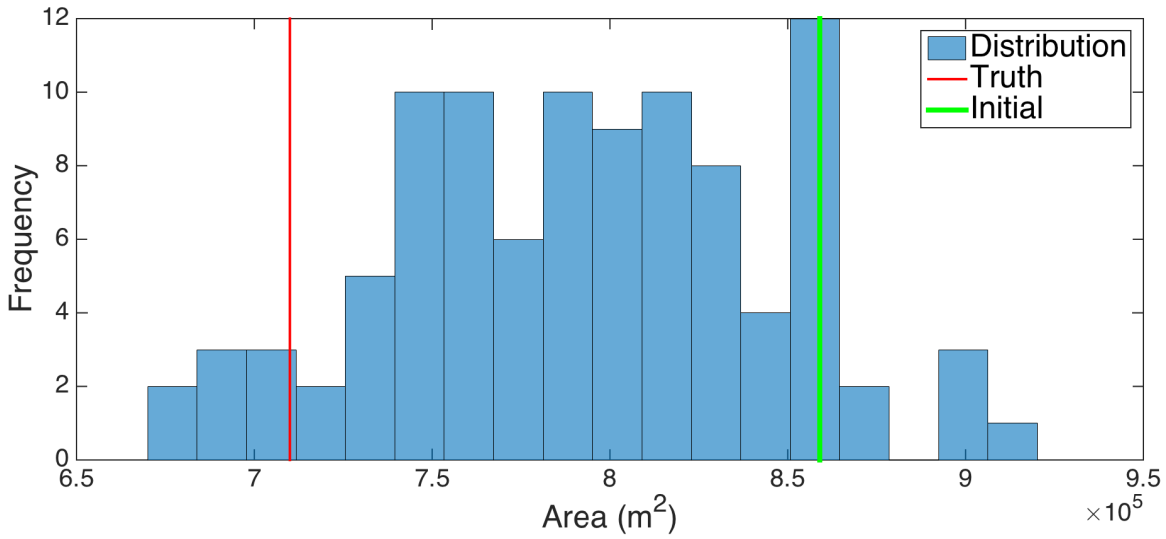


Figure 10: Distribution of the size of the region of interest over the entire set of images generated from our set of velocity models.

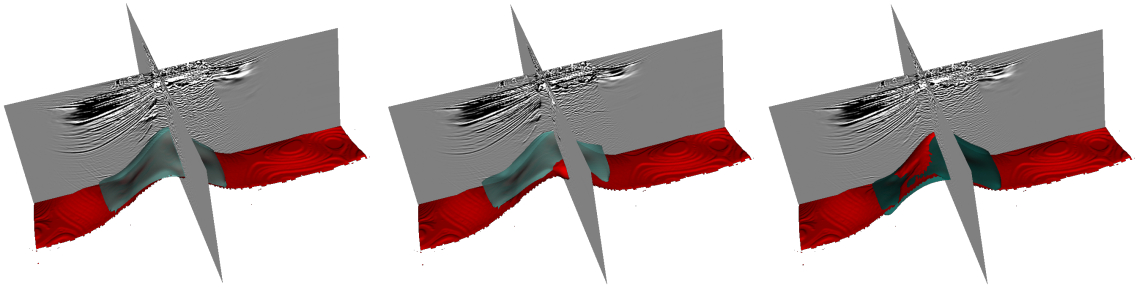


Figure 11: Manual 3D interpretation of structure in green (left), and automatically generated alternative interpretations obtained using the Demons algorithm (center/right). The true structure position is shown in red.

CONCLUSION

Uncertainties in seismic imaging may have large effects on reservoir forecasting and decision-making. However, due to the computational costs and technical difficulties, this source of uncertainty is frequently neglected in reservoir modeling workflows. In this paper, we present a new framework that combines geostatistics with seismic imaging, followed by human interpretation and automatic image registration to assess seismic uncertainty. In contrast with common practice today, where a preferred structural model is produced before uncertainty is considered, we instead access uncertainty directly by generating a set of alternative velocity models, and thus migrated images, that are verified against geophysical observations. To avoid the computational costs of having to migrate each model in this ensemble, a model selection step is proposed to select a representative subset. Finally, image registration combined with human input can be applied in lieu of manually interpreting each migrated image. This allows for direct linking of seismic velocity uncertainty to the positional uncertainty of imaged structures.

Our present workflow has focused on generating multiple realizations of salt geometries, and does not consider anisotropy, and the updating of subsalt sediment velocities. Future work will focus on incorporating these additional sources of uncertainty into the velocity generation process. Furthermore, integration of tomographic migration velocity analysis into the velocity model

perturbation could allow for the generation of velocity models that are directly consistent with measured geophysical data. We believe that building upon our proposed geostatistical framework, will offer the potential to greatly improve both the understanding and assessment of uncertainty throughout the reservoir forecasting and decision making process.

ACKNOWLEDGEMENTS

We would like to thank the affiliates and sponsors of the Stanford Center for Reservoir Forecasting, and of the Center for Wave Phenomena at Colorado School of Mines. We would also like to acknowledge SEG for the SEAM model.

WORKS CITED

Baysal, E., Kosloff, D. D., & Sherwood, J. W. (1983). Reverse Time Migration. *Geophysics , 48* (11), 1514-1524.

Biondo, B. (2005). *3-D Seismic Imaging.* Tulsa, OK, USA: Society of Exploration Geophysists.

Clapp, R. (2004). *Multiple realizations: Model variance and data uncertainty.* Stanford University, Department of Geophysics. Stanford: Stanford Exploration Project.

Li, L., Sava, P., & Caers, J. (2014). Uncertainty maps for seismic images through geostatistical model randomization. *SEG Technical Program Expanded Abstracts 2014* (pp. 1496-1500). Denver: Society of Exploration Geophysicists.

Mallet , J.-L. (2014). *Elements of mathematical sedimentary geology: The GeoChron model.* Houten: EAGE Publications bv.

Osypov, K., Yang, Y., Fournier, A., Ivanova, N., Bachrach, R., Yarman, C., et al. (2013). Model-uncertainty quantification in seismic tomography: method and applications. *Geophysical Prospecting , 61*, 1114-1134.

Perlin, K. (2002). Improving noise. *SIGGRAPH '02 Proceedings of the 29th annual conference on Computer graphics and interactive techniques* (pp. 681-682). New York: ACM.

Scheidt, C., & Caers, J. (2009). Representing spatial uncertainty using distances and kernels. *Mathematical Geosciences , 41* (4), 397-419.

Schroeder , M. (1991). *Fractals, Chaos, Power Laws: Minutes from an Infinite Paradise.* Mineola, New York, USA: Dover Publications.

Stoffa, P. L., Fokkema, J. T., de Luna Friere, R. M., & Kessinger, W. P. (1990). Split-step Fourier Migration. *Geophysics , 55* (4), 410-421.

Thirion , J.-P. (1998). Image matching as a diffusion process: an analogy with Maxwell's demons. *Medical Image Analysis , 2* (3), 243-260.

Thore, P., Shtuka, A., Lecour, M., Ait-Ettajer, T., & Cognot, R. (2002). Structural uncertainties: Determination, management, and applications. *Geophysics , 67* (3), 840-852.

APPENDIX

A.1 PROCRUSTES DISTANCE

The Procrustes distance measures the distance between two shapes using a measure that is invariant to shift, translation and scale. Given two shapes defined by points at coordinates (x_{j1}, y_{j1}, z_{j1}) and (x_{j2}, y_{j2}, z_{j2}), the algorithm proceeds in four steps:

1. Compute centroid of each shape, and compute translation between the centroids:

$$(\bar{\boldsymbol{x}}, \bar{\boldsymbol{y}}, \bar{\boldsymbol{z}}) = \left(\frac{\mathbf{1}}{\boldsymbol{n}} \sum_{j=1}^{n} \boldsymbol{x_j}, \sum_{j=1}^{n} \boldsymbol{y_j}, \sum_{j=1}^{n} \boldsymbol{z_j} \right)$$

2. Use Frobenius norm as shape size metric to compute scale the shapes as required:

$$\boldsymbol{S(x)} = \sqrt{\sum_{j=1}^{n} [(\boldsymbol{x_j} - \bar{\boldsymbol{x}})^2 + (\boldsymbol{y_j} - \bar{\boldsymbol{y}})^2 + (\boldsymbol{z_j} - \bar{\boldsymbol{z}})^2]}$$

3. Compute optimal rotation to superimpose the two shapes. If $\mathbf{x}_1$ and $\mathbf{x}_2$ are *n* x *3* matrices containing shape coordinates, we apply a SVD to $\mathbf{x}_1^T\mathbf{x}_2$ to obtain $\mathbf{UDV}^T$, the rotation matrix is then given by $\mathbf{VU}^T$.
4. Apply the transformations computed in previous three steps. The Procrustes distance is defined as the sum of squared point distances of the shapes after transformation

$$\boldsymbol{P_d^2} = \sum_{j=1}^{n} [(\boldsymbol{x_{j1}} - \boldsymbol{x_{j2}})^2 + (\boldsymbol{y_{j1}} - \boldsymbol{y_{j2}})^2 + (\boldsymbol{z_{j1}} - \boldsymbol{z_{j2}})^2)]$$

A.2 PHASE CORRELATION

Phase correlation is used to estimate the translation between two images. It is performed in the frequency domain for computational efficiency. For two images s_1 and s_2, the algorithm proceeds as follows:

1. Calculate discrete Fourier transform of both images:

$$S_1 = \mathcal{F}(s_1), S_2 = \mathcal{F}(s_2)$$

2. Calculate the cross-power spectrum by multiplying the Fourier transform of the first image by the complex conjugate of the second, and normalizing:

$$D = \frac{S_1 \circ S_2^*}{|S_1 \circ S_2^*|}$$

3. Compute the normalized cross-correlation by taking the inverse Fourier transform:

$$d = \mathcal{F}^{-1}(D)$$

4. The translation is estimated to be:

$$(\Delta x, \Delta y, \Delta z) = argmax_{(x,y,z)}(d)$$